Ballistic transport and boundary scattering in InSb/In_{1-x}Al_{x}Sb mesoscopic devices

A. M. Gilbertson, M. Fearn, A. Kormányos, D. E. Read, C. J. Lambert, M. T. Emeny, T. Ashley, S. A. Solin, and L. F. Cohen

Phys. Rev. B **83**, 075304 — Published 8 February 2011

DOI: 10.1103/PhysRevB.83.075304

Ballistic transport and boundary scattering in $InSb/In_{1-x}Al_xSb$ mesoscopic devices

A. M. Gilbertson,[1*] M. Fearn,[2] A. Kormányos,[3] D. E. Read,[1] C. J. Lambert,[3] M. T. Emeny,[2] T. Ashley,[2] S. A. Solin[1,4] and L. F. Cohen[1]

[1]*Blackett Laboratory, Imperial College London, Prince Consort Rd., London, SW7 2BZ, UK*

[2]*QinetiQ, St. Andrews Road, Malvern, Worcestershire, WR14 3PS, UK*

[3]*Department of Physics, Lancaster University, Lancaster, LA1 4YB, UK*

[4]*Center for Material Innovations and Department of Physics, Washington University in St. Louis, Saint Louis, MO-63130, USA*

*Corresponding author: adam-maurick.gilbertson@ic.ac.uk

We describe the influence of hard wall confinement and lateral dimension on the low temperature transport properties of long diffusive channels and ballistic crosses fabricated in an InSb/$In_{1-x}Al_xSb$ heterostructure. Partially diffuse boundary scattering is found to play a crucial role in the electron dynamics of ballistic crosses and substantially enhance the negative bend resistance. Experimental observations are supported by simulations using a classical billiard ball model for which good agreement is found when diffuse boundary scattering is included.

I. INTRODUCTION

The InSb two dimensional electron gas (2DEG) is attractive for room temperature (RT) applications such as high speed logic devices[1] and high spatial resolution magnetic field sensors[2] where carrier mobility plays an important role. Recent improvements in the growth of InSb/$In_{1-x}Al_xSb$ quantum wells (QWs) on GaAs substrates have lead to RT electron mobility values in excess of $\mu = 6$ m^2/Vs approaching the phonon limited value of 7 m^2/Vs.[3] For applications requiring high spatial resolution, device miniaturization inevitably leads to the relevant lateral dimensions of the conducting channel becoming comparable to the elastic mean free path ($\lambda_{0,}$) where transport is ballistic. In this regime the bulk properties of the 2DEG are no longer preserved. Therefore, it is essential to understand how the InSb 2DEG properties are altered when fabricated at the nanoscale. For example, in long InAs/AlSb 2DEG channels fabricated using reactive ion etching (RIE) the mobility is degraded from that in the bulk due to top surface damage caused by energetic ions, but the RIE-induced sidewall roughness degrades the mobility further as the width of the channel (w) is reduced below λ_0 owing to electron-boundary scattering.[4] Degradation of μ is detrimental to the performance of transistors, conventional Hall, and extraordinary magnetoresistor (EMR) sensors based on diffusive transport, but it is not clear how properties are further effected in the mesoscopic regime. Here we present a comprehensive study on the effect that fabricating high mobility InSb/InAlSb structures with critical dimensions less than the mean free path has on the transport properties.

When the length of the channel (l) is reduced below the mean free path ($l < \lambda_0$), electrons can traverse the device without scattering internally. Ballistic transport in

GaAs/$Al_xGa_{1-x}As$ microjunctions (where. $l,w < \lambda_0$) has been widely studied at low temperatures and using the Landauer-Büttiker (L-B) formalism[5] a good understanding of the phenomena is established.[6, 7] In particular, a variety of distinct departures from classical behaviour appear in the low field magnetotransport of simple cross junctions, such as a negative resistance in zero magnetic field referred to as "bend resistance",[8, 9] and a quenched or negative Hall resistance at low fields.[10] The above mentioned anomalies, at least when the number of transverse modes, N, is much larger than one ($N >>1$), can be adequately described by combining the L-B formalism and a classical approach, whereby electrons are treated as classical particles which, in analogy to ray optics, reflect from the boundaries with predicable trajectories.[11]

Lateral depletion of conducting channels, or sidewall depletion, is also relevant as devices are miniaturized. With the exception of the InAs system that exhibits very little sidewall depletion,[12] Fermi level pinning at the surface of mesa etched III-V devices can lead to substantial sidewall depletion, which is often not straightforward to deduce. Knowledge of the depletion width (w_{dep}) is essential in order to determine the true *effective* electrical width (w_{eff}) of narrow channel devices e.g. sub-micron Hall sensors[13] and quasi-1D wires[14]

The mesoscopic properties of InSb and its heterostructures is still relatively unexplored.[15] Negative bend resistance (NBR) was reported in InSb/$In_{1-x}Al_xSb$ sub-micron structures up to $T \leq 205$ K.[16] It was proposed that parallel conduction in the heterostructure masks the ballistic component from the 2DEG. Indeed, a recent study of transport in similar InSb/$In_{1-x}Al_xSb$ samples showed that at elevated temperatures intrinsic conduction in the ternary buffer layer contributes up to ≈5% of the total conduction.[17] The significance of such parallel conduction is accentuated in shallow etched sub-micron structures where the volume of remaining buffer layer is large. This

technological problem may be overcome by improved heterostructure design. Therefore, two regimes are identified in InSb/$In_{1-x}Al_xSb$ sub-micron structures (a) low temperatures (< 100 K), where ballistic transport in the 2DEG is dominant and (b) high temperatures (>150 K) where as yet, in all reported structures, parasitic intrinsic conduction in the buffer layer occurs.

We emphasise that the interaction of charge carriers with the device boundaries plays a central role in determining the characteristics of sub-micron devices and a proper investigation in the InSb 2DEG system has not been made; in particular, ballistic anomalies are acutely sensitive to the device dimension, geometry,[18] and the specularity of the boundary scattering.[19, 20] Accordingly, we report here a detailed study of the influence of device size, sidewall depletion, and boundary scattering on the magnetotransport properties of InSb/$In_{1-x}Al_xSb$ mesoscopic structures with hard wall confinement. For the purpose of this article, we present data from long channels ($l > \lambda_0$) and sub-micron crosses with lateral dimensions down to $w \approx 170$ nm, and we restrict ourselves to low temperatures where intrinsic conduction is negligible. A detailed analysis of the ballistic transport anomalies and the agreement with theory is presented with the aid of a classical billiard ball model.

II. EXPERIMENTAL METHODS

Devices were fabricated from a single modulation doped InSb/$In_{1-x}Al_xSb$ QW heterostructure grown by molecular beam epitaxy onto a GaAs (001) substrate. In growth sequence, the sample consists of an AlSb (200 nm)/$In_{0.9}Al_{0.1}Sb$ (3 μm) buffer layer, a 30 nm InSb QW and, a 50 nm $In_{0.85}Al_{0.15}Sb$ cap in which a single Te δ-doping layer is located, 20 nm above the top of the QW. Fig. 1(d) shows the self consistent

Schrödinger-Poisson solution for the conduction band profile and the energy levels in the QW. The properties of the as-grown 2DEG were determined from a 40 μm wide Hall bridge (control sample) fabricated using conventional wet etching. At 2 K the 2D electron density (n) and mobility (μ) were n = 3.95x10^{15} m^{-2} and μ = 19.5 m^2/Vs, corresponding to a mean free path of $\lambda_0 = \hbar k_F \mu / e$ = 2.03 μm and a Fermi wavelength of 40 nm [$k_F = (2\pi n)^{1/2}$ is the Fermi wavevector]. The bulk magnetotransport properties of this and similar samples were recently reported. At low temperatures relevant to this study, the mobility was found to be limited by remote ionised impurity scattering from the Te δ-layer.[3, 17] Measurements were performed with the sample in the dark using a low-frequency lock-in technique (currents between 100 and 500 nA) and with B applied perpendicular to the plane of the 2DEG.

Hall crosses and Hall bridges with varying w were patterned by electron beam lithography using negative tone resist as an etch mask. Pattern transfer was achieved using an inductively coupled plasma-RIE in a CH_4/H_2 gas mixture at a pressure of 10 mTorr, forming shallow mesas of ≈135 nm depth that provide hard wall confinement. The process parameters yielded an etch rate of the ternary $In_{0.85}Al_{0.15}Sb$ compound of ≈10 nm/min. Ti/Au Ohmic contacts were made using standard optical lithography and a cold shallow contacting technique.[21] A deep wet chemical etch was used to remove the entire 3 μm thick buffer layer surrounding the device and contacts; the volume of remaining buffer layer beyond the shallow boundaries of the structures was minimised by mask design and controlled lateral etching [see Fig. 1(a)]. Electron micrographs of a w = 171±10 nm cross and w = 550±10 nm Hall bridge are shown in Fig. 1(a) and (b) [the uncertainty in w is due to residual polymer deposit from the RIE at the mesa edge (fencing)]. The junction corners are nominally square, but a small unavoidable rounding

of the corners (< 50 nm radius) results from the large proximity effect in the e-beam lithography of InSb.

III. CLASSICAL BILLIARD BALL MODEL

To interpret our results presented in the following section, we simulate the bend and Hall resistance of the cross junction following the classical model of Beenakker and van Houten that treats electrons as classical particles (billiard balls) reflecting from the device boundaries.[11] The resistance in the ballistic regime is expressed in terms of the transmission probabilities between the various leads by the L-B formula.[5] We consider the four-terminal cross geometry with four-fold symmetry, in which case, respectively the Hall and bend resistances, R_H and R_B are given by:

$$R_H = R_0 \frac{T_R^2 - T_L^2}{(T_R + T_L)[(T_R + T_F)^2 + (T_L + T_F)^2]} \tag{1a}$$

and

$$R_B = R_0 \frac{T_L T_R - T_F^2}{(T_R + T_L)[(T_R + T_F)^2 + (T_L + T_F)^2]} \tag{1b}$$

where T_F, T_L and T_R are the probabilities of an electron transmitted from the injection lead (arbitrary) to the forward, left and right hand leads respectively, and $R_0 = h/2e^2N$ with N equal to the number of transverse modes at the Fermi energy. The geometry of the cross junction is shown in Fig. 1(c) and is defined by three parameters: the lead width w, lead length l' and radius of curvature of the corners, r, with $r^2=x^2+y^2$ in the plane. For the purposes of our calculations, we use a hard wall confining potential (infinite potential barriers at the boundaries). This is a good approximation for wider

leads, greater than 200 nm in width, in which the potential is very flat in the centre of the channel and increases rapidly near the boundaries.[22] In the semiclassical limit and for hard wall confinement, N is given by $N = k_F w/\pi$. All calculations presented are for $N >> 1$, where the model is strictly valid.

The transmission and reflection coefficients are calculated by injecting a large number of classical particles ($5x10^4$) from a specified injection lead uniformly across the lead with an angular distribution $P(\phi) = \frac{1}{2}\cos(\phi)$ (ϕ being the angle with respect to the lead axis).[11] The trajectories of the particles are determined via integration of the equations of motion using the Verlet technique until they exit the junction via one of the four leads. Particles are injected into the junction region at the Fermi velocity $v_F = \hbar k_F / m^*(E)$ with an effective mass $m^*(E)$ which takes into account the modifications due to band non-parabolicity within an analytical model for the dispersion, $E(1+\alpha E) = \hbar^2 k^2 / 2m^*$ where α is non-parabolicity parameter.[23] For the InSb QW studied here we use a subband edge effective mass m_{sb}^*=0.0162 and a non-parabolicity parameter of α = 3.8 eV^{-1} which gives a fit to an 8 band k.p model of a 30 nm QW with $In_{0.85}Al_{0.15}Sb$ barriers to within a few meV over a 100 meV range.

We incorporate diffuse boundary scattering into the model using the approach of Blaikie *et al.*[20]. Boundary scattering is captured using a single specularity parameter, p, that describes the probability of a particle scattering diffusively (1 - p) from a boundary. After a diffuse scattering event, particles are re-injected at the collision point with an angle $-\pi/2 \leq \theta \leq \pi/2$ from the boundary normal chosen randomly from a uniform distribution. Within this model, the transmission coefficients are sensitive to the lead length *l'* as this directly affects the number of interactions with the boundary.

IV. RESULTS AND DISCUSSION

A. Diffuse properties in long channels

Fluctuations in the electrostatic potential profile of a conducting channel can alter the transport properties via electron-boundary scattering, particularly in sub-micron devices where the channel width $w \leq \lambda_0$ and electrons can travel ballistically between the channel boundaries.

Electron-boundary scattering can be characterised by two parameters; the specularity parameter p and λ_B, the average distance an electron travels before the probability of it scattering diffusely is equal to one.[19] In general $p < 1$ for both mesa etched and split-gate devices.[19, 24] λ_B is proportional to w, so that as w is reduced the electron-boundary interactions manifest in the transport properties. The increased backscattering in narrow channels enhances the zero-field longitudinal resistance $R_{xx}(0)$, resulting in an effective μ that is reduced from that in a wide sample. For partially diffuse scattering ($p < 1$), a distinctive low field peak appears in the $R_{xx}(B)$ (discussed in Section IVC).[7]

Measurements were performed on long channels in the Hall bridge geometry (Fig. 1(b) and inset to Fig. 2) with a longitudinal voltage lead separation of l = 8.4 μm ($> \lambda_0$) ensuring that transport is diffusive along the channel. In Fig. 2 we show the longitudinal R_{xx} and transverse R_{xy} resistance as a function of magnetic field at 2 K for a 3 μm and 550 nm wide Hall bridge. Shubnikov de-Haas (SdH) oscillations in R_{xx} are observed in each device superposed onto an increasing background resistance related to parallel conduction in the upper barrier.[17] The 2D electron density n is determined from the periodicity of SdH oscillations and the mobility μ from the zero field resistance, according to $\mu = l / wR_{xx}(0)ne$. The experimental n, μ and the corresponding mean free paths for the w = 3 μm and 550 nm Hall bridges are given in Table I, together with the

properties of the control sample (w = 40 μm). A monotonic decrease in n and μ is observed as w is reduced. The reduction in n is attributed to the lateral potential formed by a sidewall depletion region (discussed further in the section IVB) in addition to the lateral confinement imposed on narrow channels which raise the conduction band edge in the centre of the channel as w is reduced, hence depleting the 2DEG. The observed degradation of μ is consistent with the presence of boundary scattering which becomes increasingly important as w is reduced. Nevertheless, the mobility in the 550 nm wide channel is only degraded by ≈25 % with respect to the control sample, with a corresponding mean free path of λ_0 = 1.5 μm. Ballistic transport is therefore expected in the sub-micron crosses ($\lambda_0 > w$) discussed in Section IVD.

B. Determination of depletion width

An important parameter of narrow channels is the electrical width w_{eff}. Due to the Fermi energy pinning in the band gap at the air-interface, sidewall depletion is frequently observed for narrow mesa-etched channels resulting in a w_{eff} that can be substantially smaller than the physical width, w.[25,14] The difference is equal to the sum of the lateral depletion width at each boundary (w_{dep}). Knowledge of w_{dep} is essential for many applications but is not straightforward to gain. We found that devices with $w \leq$ 134 nm were electrically depleted over the entire temperature range. This puts an initial estimate on the depletion width at $w_{dep} \approx$ 67 nm. We determine w_{eff} from tracking the depopulation of quasi-1D magnetoelectric subbands in the low field R_{xx} data of narrow channels.[26] Like 2D Landau levels, these hybrid subbands depopulate with increasing field, but do so at a slower rate as evidenced by a non-linear subband index (i) versus

1/*B* plot in the low field region. For a parabolic confining potential, the magnetic depopulation of subbands can be described analytically by[26]

$$i \approx \left[\frac{3\pi}{4} N_{1D} \omega_0 \left(\frac{\hbar}{2m^*} \right)^{1/2} \right]^{2/3} \frac{1}{\omega} \qquad (2)$$

where N_{1D} is the 1D electron density, ω_0 is the characteristic frequency defining the strength of the confinement and $\omega = \left(\omega_c^2 + \omega_0^2\right)^{1/2}$ where $\omega_c = eB/m^*$ is the cyclotron frequency. One can see that for small fields, the dependence of *i* on 1/*B* is non-linear and for large fields, $\omega \to \omega_c$ and *i* is proportional to 1/*B* as in the usual 2D case. As noted in Ref. 26, a square well potential is more appropriate for wider channels, nevertheless, the model expressed in Eq. 2 provides valuable insight to the effective width of the channel. A subband depopulation diagram for the *w* = 550 nm Hall bridge is shown in Fig. 3. A pronounced departure from linear in 1/*B* behaviour (dashed line) is observed below 1 T. The solid line in Fig. 3 represents a least squares fit of Eq. 2 to the data using an effective mass at the Fermi energy of $m^*=0.022m_0$ (we found that the fitting results are relatively insensitive to small changes of ±10% in *m**). From this fit we deduce a confinement energy $\hbar\omega_0$ and N_{1D} of 2.6 meV and $3\text{x}10^9$ m^{-1}, respectively. The effective width is then estimated from[26]

$$w_{eff} = 2\pi N_{1D}^{1/3} \left(\frac{2\hbar}{3\pi m^* \omega_0} \right)^{2/3} \qquad (3)$$

Substituting the values of ω_0 and N_{1D} into Eq. 3 we determine w_{eff} = 414 nm ± 5 nm. This implies a depletion width of $w_{dep} = (w-w_{eff})/2$ = 68 nm ± 6 nm which is in

remarkably good agreement with the estimate made directly from the observed electrical depletion of devices of $w < 134$ nm.

Finally, we remark on a separate and consistent estimate of w_{eff} made from a classical size effect (with no assumption of confining potential). Electron backscattering in narrow channels that enhances $R_{xx}(0)$ is suppressed by a perpendicular magnetic field due to the formation of localised edge states or classical skipping orbits at the boundaries. This leads to a negative MR peaked at $B = 0$, persisting until $B_{min} = 2B_0$, where $B_0 = \hbar k_F / e w_{eff}$ is the field when the cyclotron radius, $R_c = \hbar k_F / eB$, equals w_{eff}, at which point a marked change in slope is expected.[27] As seen in Fig. 2 (and more clearly in Fig. 4), this behaviour is observed in our data. A kink in the low field MR is observed at a field $B_{min} \approx 0.5$ T (indicated by an arrow), from which we estimate $w_{eff} \approx$ 406 nm (i.e. $w_{dep} \approx 72$ nm). This estimate is consistent with the value obtained from the magnetodepopulation analysis, adding confidence to our estimate of w_{dep}.

C. Partially diffuse boundary scattering in narrow channels

The specularity of the boundary scattering plays a crucial role in the transport of submicron devices. In particular, Blaikie *et al.*[20] showed that resistance anomalies in ballistic devices can be substantially enhanced by partially diffuse boundary scattering. The specularity of boundary scattering can be studied from measurements on long narrow channels ($w \leq \lambda_0$) where electron-boundary interactions manifest in the resistance. It has been shown that partially diffusive boundary scattering leads to an anomalous peak in R_{xx} at small fields ($0 < B < B_{min}$) with a position (B_{max}) that scales inversely with w.[19, 28, 29] As seen in Fig. 2 a pronounced peak is distinguished in the low field R_{xx} of the $w = 550$ nm Hall bridge at $B_{max} \approx 180$ mT (indicated by the arrow). We

note that a low field peak with entirely different origin was also predicted[11] and experimentally observed[30] in the MR of ballistic Hall bridges where $l < \lambda_0$. In our case, $l >> \lambda_0$ so that the measurement is in the diffusive regime and the observed peak is unambiguously attributed to partially diffuse boundary scattering.

In Fig. 4 we show the low field MR of the w = 550 nm Hall bridge $[R_{xx}(B)-R_{xx}(0)]/R_{xx}(0)$ plotted against the normalised field B/B_0 (using w_{eff} = 414 nm) at various temperatures between 2 K and 80 K after subtraction of the high field quasi-linear background. The classical model for in-plane MR of thin metal films (where the film thickness $t \leq \lambda_0$ and $p = 0$) predicts that $B_{max} = 0.55B_0$ i.e. when $R_c = w_{eff}/0.55$. This has previously been considered as a method of estimating w_{eff}.[28-30] We have found that the boundary scattering peak occurs at a somewhat larger value $B_{max} \approx 0.7B_0$. It follows that estimating w_{eff} from the classical prediction[28] $w_{eff} = 0.55R_c$ yields a value significantly less than that obtained in the previous section. Given that the calculations of B_{max} are sensitive to the details of the model[30] and that predicted values have been reported in the range $0.55B_0 \leq B_{max} \leq B_0$,[30, 31] we suggest that this method provides a less reliable estimate of w_{eff}.

The decay of the peak at B_{max} with temperature is associated with the reduction of λ_0 in the bulk of the channel (taken from the control device where boundary scattering can be neglected) below λ_B.[19] The boundary scattering length is estimated (rather arbitrarily) by assuming that $\lambda_B \approx \lambda_0$ (in the bulk of the channel) at the temperature (T') when $\Delta R_{xx}(B_{max})/R_{xx}(0) = 1$.[24] Taking T' ≈ 40 K corresponds to $\lambda_B \approx$ 1.75 μm. The specularity parameter p is then estimated from the empirical relationship $1 - p \approx w_{eff}/\lambda_B$ yielding $p \approx 0.71$ for the w = 550 nm (w_{eff} = 414 nm) Hall bridge. The inset of Fig. 4 shows the amplitude of the peak at B_{max} plotted against λ_0 obtained from the control sample at each temperature. The amplitude was extracted with respect to a

straight line drawn between data at $B/B_0 = 0$ and $B/B_0 = 2$. Using this plot, λ_B may be interpreted as the value of λ_0 when the peak amplitude decays to zero. Two dependences on λ_0 are distinguished in the data, a rapid decay (solid line) labelled as A and a slower decay (dashed line) labelled as B. We broadly separate these into the regimes where remote ionized impurities and phonons dominate momentum scattering in the bulk of the channel, respectively. We consider regime B unsuitable for this analysis since large angle phonon scattering randomises the electrons' momentum in addition to diffuse boundary scattering events which alter λ_B. Therefore, only at low temperatures (regime A) can information on λ_B be extracted with confidence. In regime A, we extrapolate a value of $\lambda_B \approx 1.85$ μm, giving $p \approx 0.77$ which is similar to the previous estimate. We conclude from our analysis that $p \approx 0.7$ - 0.8.

The value of p is expected to be a property of the boundaries themselves and therefore be the same for devices fabricated in the same way. Given the assumptions made to estimate p, emphasis should not be on the value of p itself but rather it should be sufficient that one observes the characteristic low field MR features shown in Figs. 2 and 4, to conclude that partially diffuse boundary scattering is significant and $p < 1$.

D. Ballistic transport in cross junctions

We now turn to the experimental results in ballistic crosses formed from two intersecting channels of width w [see inset to Fig. 1(a)], where the relevant lateral dimensions $L \approx w$ are substantially less than the mean free path. We present the results from four crosses with physical widths (inferred from SEM inspection) of $w = 924$, 550, 400, and 171 nm ± 10 nm. The inferred effective electrical widths $w_{eff} = w - 2w_{dep}$ are given in Table II where we have used the depletion width determined in Section IVB

(w_{dep} = 68 nm). Note that the smallest cross (w = 171 nm) has an estimated electrical width of $w_{eff} \approx$ 35 nm which is among the narrowest conducting mesa-etched devices reported.[12]

Figure 5 shows the results for the Hall resistance $R_H = V_{4,2}/I_{1,3}$ [the lead arrangement is shown in Fig. 1(a)] as a function of B for the crosses. Here V_{ij} and I_{mn} indicate the voltage of terminal i measured with respect to j when current is passed from terminal m to n, respectively. Data for w = 924 nm, 550 nm, and 400 nm were taken at 2 K and the w = 171 nm at 40 K (the w = 171 nm junction became depleted for T < 30 K). Quantum Hall plateaus are resolved in the data from the largest three crosses. The electron densities are determined from fits of the classical 2D result $R_H(B) = -B/ne$ (indicated by the dashed lines in Fig. 5) to the high field linear portions of data. $R_H(B)$ for the w = 171 nm cross is strikingly different - no obvious quantisation of R_H occurs over the entire field range and $R_H(B)$ is non-linear up to $|B| \approx 4$ T making the determination of n less trivial. The extracted electron densities of the crosses are listed in Table II. The dependence of n on w_{eff} is presented in the bottom inset to Fig. 5 including data from wider Hall bridges.

At low fields $|B| < 1$ T, clear anomalies appear in R_H for all crosses (top inset to Fig. 5) - the development of the anomalies with decreasing w is clear. No suppression of R_H around $B = 0$ is observed in the largest three crosses (a very small reduction is found for the w = 400 nm cross). In the smallest cross (blue line) the effect is striking; R_H is completely quenched *and negative* (positive in our configuration) up to $|B| < 0.65$ T. A small asymmetry in $R_H(B)$ is observed in all cases which is attributed to geometric asymmetries in the junction. The appearance of quenching is of interest with respect to the geometry of the junction. Baranger and Stone[32] showed that generic quenching of R_H occurs only in junctions with rounded corners; a consequence of a horn collimation

effect[33] that results in a non-equilibrium momentum distribution that enhances the forward transmission (T_F) at the expense of the transmission into the left (T_L) and right (T_R) leads [c.f. Eq. 1(a)]. Electron collimation was experimentally verified by Molenkamp *et al.*[34] and is a key concept in describing ballistic anomalies as we demonstrate here. Likewise, the negative R_H results from rebound trajectories (directing electrons into the 'wrong' lead for a given field direction) that are only effective in rounded junctions when the radius of curvature of the junction corner (r) is large compared to the lead width i.e. $r/w > 1$.[35,18] The appearance of these features in the w = 171 nm cross is therefore a clear signature of both significant rounding and collimation. Conversely, the lack of quenching in the largest three crosses implies that r/w_{eff} is small i.e. the junctions are approximately square as intended. In this respect the apparent rounding in the 171 nm cross is perhaps surprising; however, if we assume that r must be at least w_{dep}, then the lower bound for r is ≈ 70 nm. In this case $r/w_{eff} > 1$ for the smallest cross and < 1 for the larger crosses, in agreement with our observations. Some small additional rounding is inevitable in the e-beam and etch process [< 50 nm radius from the inset to Fig. 1(a)], putting our experimental estimate of r at 120 nm > r > 70 nm.

Beyond the quenched region, R_H rises above its classical value (dashed lines in Fig. 5) in all devices, marking the onset of the classical 'last plateau'.[10, 18] At larger fields still, $R_H(B)$ rejoins the classical Hall resistance (indicated by the arrows in Fig. 5). For the w = 171 nm cross the non-linearity persists up to $|B| \approx 4$ T. The sharp rise in $R_H(B)$ above its classical value results from trajectories that *guide* electrons into a side lead with minimal boundary reflections thereby enhancing the asymmetry between T_L and T_R.[11] When guiding is fully effective, electrons are no longer reflected back into the junction (skipping orbits along the junction perimeter) and $T_F, T_R << T_L \approx 1$. With

reference to Eq. 1(a), in this regime $R_H(B)$ is predicted to plateau at a value equal to the contact resistance of the lead $R_0 = h/2e^2N$. Classical behaviour is then recovered $B \geq 2B_0$. Although a clear plateau region is not observed in our experimental data, features consistent with the predictions of the classical model are observed. For example, the estimated value $2B_0 = 4.5$ T for the $w = 171$ nm cross coincides approximately with the field at which the experimental data rejoin the classical Hall slope. Similar agreement is found for each cross indicating that our estimations of w_{eff} and k_F are close to their true values (R_0 and B_0 for each cross are listed in Table II).

In Fig. 6(a) we show low field results obtained in the bend resistance configuration $R_B = V_{4,3}/I_{1,2}$ for the crosses (again, data for the $w = 171$ nm cross was obtained at 40 K). A substantial NBR peak centred about $B = 0$ is observed in all devices that increases as w is reduced. Asymmetries in the field dependence are also observed in this configuration and are particularly evident in the data for $w = 400$ nm cross [solid black line in Fig. 6(a)]. To ascertain the origin of the asymmetries, measurements were repeated with the current and voltage leads interchanged. Representative data for the $w = 400$ nm cross is shown by the dashed black line in Fig. 6(a). One can see that the reciprocity relation $R_{mn,ij}(B) = R_{ij,mn}(-B)$ is obeyed demonstrating that the field asymmetries indeed originate from asymmetries in the junction geometry.[5] This is representative of each device measured.

The origin of NBR is well established: it arises from 'straight through' trajectories which raise the potential at lead 3 with respect to lead 4 [see Fig. 1(a)], resulting in a negative resistance. This corresponds to $T_F >> T_L, T_R$ in the L-B formula [c.f. Eq. 1(b)]. In a small magnetic field the Lorentz force curves the trajectories into the 'correct' lead 4 and the NBR decays to zero producing a characteristic negative peak (for $B > 0$ this corresponds to $T_R = T_F = 0$). In our case, a small diffuse background

resistance is present ranging from 20-30 Ω (discussed further in Section IVE). Before the background resistance is recovered, a small 'overshoot' of positive resistance is observed in each cross [indicated by the arrows in Fig. 6(a)] due to rebound trajectories, in rounded junctions, that briefly increase the transmission into the opposite lead. This coincides with the rise in R_H to the last plateau.

The case of NBR in zero magnetic field is useful because the solutions to the L-B formulae are simplified, allowing information on the transmission probabilities and collimation to be extracted.[34] At $B = 0$, $T_L = T_R \equiv T_S$ and Eq. 1(b) reduces to $R_B(0)/R_0 = (1-T_F/T_S)/[4(T_S+T_F)]$. For symmetric hard walled junctions with a fixed geometry (i.e. fixed r/w), the classical model[33] predicts a universal scaling of resistance curves when normalised by R_0 and B_0. In other words, the transmission coefficients (and hence collimation) are approximately equal for geometrically equivalent junctions, and $R_B(0)$ scales inversely with the number of channels $N = k_F w_{eff}/\pi$ (see Table II). For the purpose of analysis, we define an NBR amplitude $\Delta R_B = R_B'(0) - R_B(0)$ as the difference between the interpolated background resistance at $B = 0$ and $R_B(0)$ ($R_B'(0) = 0$ in the billiard model) [see inset to Fig. 6(b)]. Figure 6(b) shows the variation of ΔR_B with $1/N$ on a log-log plot. ΔR_B scales approximately, but not exactly, with $1/N$ (indicated by the dashed line). Equally, the scaling predicts that the normalised resistance $R_B(0)/R_0$ is independent of w_{eff} and k_F. Accordingly, in Fig. 7(a) we show $\Delta R_B/R_0$ plotted against w_{eff} for our devices. Remarkably we find that $\Delta R_B/R_0$ is almost identical for the largest two crosses: The geometries in these crosses must be equivalent which is consistent with the assertion that these junctions are approximately square (i.e. r/w_{eff} is small). Scaling of these data is also found for $B > 0$ when R_B/R_0 is plotted against B/B_0 (not shown). This is not true for the two smaller crosses as evidenced by a monotonic increase of $\Delta R_B/R_0$ with decreasing w_{eff}, consistent with the presence of a small but

approximately constant rounding that becomes increasingly significant as w_{eff} is reduced. These observations provide valuable insight into the geometry of the junctions which is used in the billiard model calculations presented in section IVE.

E. Simulation results

To explore further the electron dynamics within the cross junctions, calculations of the bend resistance were performed using the classical model described in Section III. Classical and quantum mechanical calculations of ballistic anomalies in microjunction have previously been performed by various authors[6, 11, 30, 36] and as discussed in these works, the geometry of the junction determines the magnitude and character of the resistance anomalies. The parameters in the calculations are w, r, l', v_F, and p (a schematic of the cross geometry is repeated in Fig. 7(a) inset for clarity). v_F is set by the experimentally determined k_F, and $w \equiv w_{eff}$ in the model (see Section III). We start by considering the magnitude of the experimental NBR and its implications on the collimation in the crosses, and then compare our results for $R_B(B)$ with experimental data.

Simulations of $\Delta R_B(0)/R_0$ for a square ($r/w = 0$) and rounded junction ($r/w = 2$) with specular boundary scattering ($p = 1$) are shown by the solid lines in Fig. 7(a). Recall that no collimation occurs in the square junction, when $p = 1$, whereas collimation is induced in the rounded junction via the horn effect. The experimental $\Delta R_B(0)/R_0$ of the two largest crosses (which we expect to be approximately square) exceeds the calculated values for a square junction by factor of ~4 and even a rounded junction by a factor of ~2. The anomalously large NBR implies additional collimation is present other than the horn effect which we attribute to the *diffuse collimation* effect[20]

that results from partially diffuse boundary scattering ($p < 1$) in our devices (as shown in Section IVC). The origin of diffuse collimation is the increased backscattering of electrons that enter the leads with large angles ϕ with respect the lead axis. Therefore, electrons injected with a ½cos(ϕ) distribution arrive at the junction region after traversing a lead of length l' with a distribution more strongly peaked in the forward direction (hence increasing the ratio T_F/T_S). The resulting angular distribution differs from the horn effect result in that it is more sharply peaked in the forward direction.[30] Consequently, the NBR for $p < 1$ has a distinctively sharper and more triangular shape about $B = 0$ than in the $p = 1$ case. In support of this conjecture, the experimental data in Fig. 6(a) exhibit the characteristic sharp NBR associated with diffuse collimation.

Billiard simulations with $p < 1$ were implemented using the approach of Ref. 20 (see Section III for details). To illustrate the enhancement of the NBR from diffuse collimation Fig. 7(a) shows a calculation of $\Delta R_B(0)/R_0$ for a square junction with $p = 0.7$ and $l'/w = 3$, as indicated by the dashed line. Remarkably, even for a square junction, the NBR amplitude is increased by a factor of ~5 over the $p = 1$ case, using reasonable parameters. Diffuse collimation is sensitive to the ratio l'/w since this directly influences the number of boundary collisions. In our devices we define l' as the length from the junction to the point at which the lead width flares out [e.g. see Fig. 1(a)]. These values are listed in Table II. Therefore, we can simulate the whole $R_B(B)$ curve using experimentally determined parameters n, w_{eff} and l' with only r and p as variables. We perform simulations of the three largest crosses where the classical model is applicable ($N >> 1$). r is estimated in the range $120 > r > 70$ nm (see Section IVD). We note that for a given w_{eff} the position and amplitude of the overshoot in R_B [indicated by the arrows in Fig. 6(a)] is quite sensitive to the value of r, and r was adjusted to best match the experimental feature. Using this method (with $p = 1$ and n,

w_{eff} and l' listed in Table II), we found that r = 100 nm yielded reasonable agreement with the experimental data for each cross. This is consistent with the fact that the unintentional rounding results from the fabrication process and sidewall depletion that is approximately independent of w. The value of p was then used as the only fitting parameter to adjust $R_B(0)$ to equal the experimental $R_B(0)$. The results of these simulations (solid red lines) are compared to the experimental data (solid black lines) in Figs. 7(b), (c) and (d). The agreement with the experimental data is excellent considering the few adjustable parameters involved, validating our experimental determination of w_{eff} and n. Corresponding simulations for p = 1 are shown for comparison by the dashed red lines in Fig. 7(b) to (d), illustrating by contrast the rounded profile of the NBR obtained in the p = 1 case. The diffuse background resistance observed in the experimental data is likely to result from the finite momentum scattering time (τ) within the crosses, implying that not all of the electrons are fully ballistic as they are treated in the model ($\tau = \infty$ in the current model). Given the agreement with the ballistic model, we speculate that any momentum scattering in the crosses does not perturb the electron trajectories considerably and therefore the extracted p parameters are meaningful. This is supported by recent work showing that at low temperatures the mobility in these InSb QWs is limited by small angle remote ionised impurity scattering i.e. not by phonon scattering that may result in additonal backscattering.[17, 37]

The values of p used for the three crosses lie range from 0.69 to 0.8 which is in good agreement with the value $p \approx 0.7$ - 0.8 estimated from the measurements on long narrow channels described in Section IVC. Moreover, the narrow range of p used in the simulations supports the claim that p is a property of the boundary and thus relatively

independent of w for devices fabricated under the same conditions. The incorporation of remote ionised impurity scattering into the billiard model is the subject of further work.

The behaviour of the ballistic anomalies described here is transferable to any material system with $p < 1$ (particularly for square cross geometries). However, we emphasise that the partially diffuse boundary scattering reported here is inextricably linked to the particular hard wall confinement we have achieved in our devices that exposes the 2DEG to the etched surface. For example, quite different specularity ($p = 1$) from mesa etched InSb narrow channels has been reported elsewhere using a different etch chemistry (note that the analysis was limited to $B = 0$).[14] In a quantum mechanical treatment of boundary scattering,[31] the proportion of diffuse scattering is dependent on the details of the boundary roughness (e.g. the amplitude and correlation length) with respect to the Fermi wavelength, which are likely to vary with the etch chemistry and extent of sidewall depletion. Therefore, it is not surprising that different etch chemistries may yield different results. Our work shows that the ballistic transport properties of InSb mesa etched devices can be well accounted for within the classical model when the sidewall depletion and realistic partially diffuse boundary scattering are properly addressed.

V. CONCLUSIONS

In summary, we have investigated the variation of the low temperature transport properties in InSb/$In_{1-x}Al_xSb$ mesa-etched mesoscopic devices with hard wall confinement when the lateral dimensions are reduced below the mean free path. Measurements on long channels and Hall crosses fabricated from the same sample show that the lateral depletion width is approximately 70 nm and that boundary

scattering from the sidewall is partially diffuse, with a specularity parameter $p \approx 0.7$ - 0.8. Ballistic crosses show characteristic resistance anomalies in good agreement with the predictions of the classical model and in all cases exhibit a significantly enhanced NBR due to partially diffuse boundary scattering from the sidewalls. Our observations are supported by classical simulations of the electron trajectories in ballistic crosses which quantitatively accounts for both the magnitude and width of the negative bend resistance, using experimentally determined parameters, and a specularity parameter p in the range 0.69 - 0.8. Our work highlights the relative importance of diffuse collimation over horn collimation. In particular, the enhancement of the NBR observed in small crosses may be of practical interest for applications requiring large responsivity e.g. high spatial resolution magnetic field sensors.

ACKNOWLEDGEMENTS

This work was supported by the UK EPSRC under Grant No. EP/F065922/1. SAS is also supported by the US NSF under Grant No. ECCS-0725538, and NIH under Grant No. 1U54CA11934201, and has a financial interest in PixelEXX, a start-up company whose mission is to market imaging arrays.

REFERENCES

[1] S. Datta, et al., in *Electron Devices Meeting, 2005. IEDM Technical Digest. IEEE International*, 2005), p. 763.

[2] S. A. Solin, D. R. Hines, A. C. H. Rowe, J. S. Tsai, Y. A. Pashkin, S. J. Chung, N. Goel, and M. B. Santos, Applied Physics Letters **80**, 4012 (2002).

[3] A. M. Gilbertson, W. R. Branford, M. Fearn, L. Buckle, P. D. Buckle, T. Ashley, and L. F. Cohen, Physical Review B **79**, 235333 (2009).

[4] K. A. Cheng, C. H. Yang, and M. J. Yang, Applied Physics Letters **77**, 2861 (2000).

[5] M. Büttiker, Physical Review Letters **57**, 1761 (1986).

[6] H. U. Baranger, D. P. DiVincenzo, R. A. Jalabert, and A. D. Stone, Physical Review B **44**, 10637 (1991).

[7] T. J. Thornton, Superlattices and Microstructures **23**, 601 (1998).

[8] Y. Takagaki, K. Gamo, S. Namba, S. Ishida, S. Takaoka, K. Murase, K. Ishibashi, and Y. Aoyagi, Solid State Communications **68**, 1051 (1988).

[9] G. Timp, H. U. Baranger, P. deVegvar, J. E. Cunningham, R. E. Howard, R. Behringer, and P. M. Mankiewich, Physical Review Letters **60**, 2081 (1988).

[10] M. L. Roukes, A. Scherer, S. J. Allen, H. G. Craighead, R. M. Ruthen, E. D. Beebe, and J. P. Harbison, Physical Review Letters **59**, 3011 (1987).

[11] C. W. J. Beenakker and H. van Houten, Physical Review Letters **63**, 1857 (1989).

[12] C. H. Yang, M. J. Yang, K. A. Cheng, and J. C. Culbertson, Physical Review B **66**, 115306 (2002).

[13] J. S. Neal, H. G. Roberts, M. R. Connolly, S. Crampin, S. J. Bending, G. Wastlbauer, and J. A. C. Bland, Ultramicroscopy **106**, 614 (2006).

[14] R. L. Kallaher, J. J. Heremans, N. Goel, S. J. Chung, and M. B. Santos, Physical Review B **81**, 035335 (2010).

[15] J. J. Heremans, H. Chen, M. B. Santos, N. Goel, W. V. Roy, and G. Borghs, Physics of Semiconductors, Pts A and B **893**, 1287 (2007).

[16] N. Goel, S. J. Chung, M. B. Santos, K. Suzuki, S. Miyashita, and Y. Hirayama, Physica E-Low-Dimensional Systems & Nanostructures **20**, 251 (2004).

[17] O. J. Pooley, A. M. Gilbertson, P. D. Buckle, R. S. Hall, L. Buckle, M. T. Emeny, M. Fearn, L. F. Cohen, and T. Ashley, New Journal of Physics **12**, 053022 (2010).

[18] C. J. B. Ford, S. Washburn, M. Büttiker, C. M. Knoedler, and J. M. Hong, Physical Review Letters **62**, 2724 (1989).

[19] T. J. Thornton, M. L. Roukes, A. Scherer, and B. P. Van de Gaag, Physical Review Letters **63**, 2128 (1989).

[20] R. J. Blaikie, K. Nakazato, J. R. A. Cleaver, and H. Ahmed, Physical Review B **46**, 9796 (1992).

[21] A. M. Gilbertson, Imperial College, 2010.

[22] S. E. Laux, D. J. Frank, and F. Stern, Surface Science **196**, 101 (1988).

[23] A. M. Gilbertson, W. R. Branford, M. Fearn, L. Buckle, P. D. Buckle, T. Ashley, and L. F. Cohen, Physical Review B (Condensed Matter and Materials Physics) **79**, 235333 (2009).
[24] M. L. Roukes, T. J. Thornton, A. Scherer, and B. P. Vandergaag, in *Electronic Properties of Multilayers and Low-Dimensional Semiconductor Structures*, edited by J. M. Chamberlain and L. Eaves (Plenum Press Div Plenum Publishing Corp, New York, 1990), Vol. 231, p. 95.
[25] H. van Houten, B. J. van Wees, M. G. J. Heijman, and J. P. Andre, Applied Physics Letters **49**, 1781 (1986).
[26] K. F. Berggren, G. Roos, and H. van Houten, Physical Review B **37**, 10118 (1988).
[27] H. van Houten, C. W. J. Beenakker, P. H. M. van Loosdrecht, T. J. Thornton, H. Ahmed, M. Pepper, C. T. Foxon, and J. J. Harris, Physical Review B **37**, 8534 (1988).
[28] A. B. Pippard, *Magnetoresistance in metals* (Cambridge Univ. Press, U.K, 1989).
[29] E. Ditlefsen, Philosophical magazine. A, Physics of condensed matter, defects and mechanical properties **14**, 759 (1966).
[30] R. J. Blaikie, D. R. S. Cumming, J. R. A. Cleaver, H. Ahmed, and K. Nakazato, Journal of Applied Physics **78**, 330 (1995).
[31] H. Akera and T. Ando, Physical Review B **43**, 11676 (1991).
[32] H. U. Baranger and A. D. Stone, Physical Review Letters **63**, 414 (1989).
[33] C. W. J. Beenakker and H. v. Houten, Physical Review B **39**, 10445 (1989).
[34] L. W. Molenkamp, A. A. M. Staring, C. W. J. Beenakker, R. Eppenga, C. E. Timmering, J. G. Williamson, C. J. P. M. Harmans, and C. T. Foxon, Physical Review B **41**, 1274 (1990).
[35] M. L. Roukes, A. Scherer, and B. P. Van der Gaag, Physical Review Letters **64**, 1154 (1990).
[36] T. Geisel, R. Ketzmerick, and O. Schedletzky, Physical Review Letters **69**, 1680 (1992).
[37] J. M. S. Orr, A. M. Gilbertson, M. Fearn, O. W. Croad, C. J. Storey, L. Buckle, M. T. Emeny, P. D. Buckle, and T. Ashley, Physical Review B **77**, 165334 (2008).

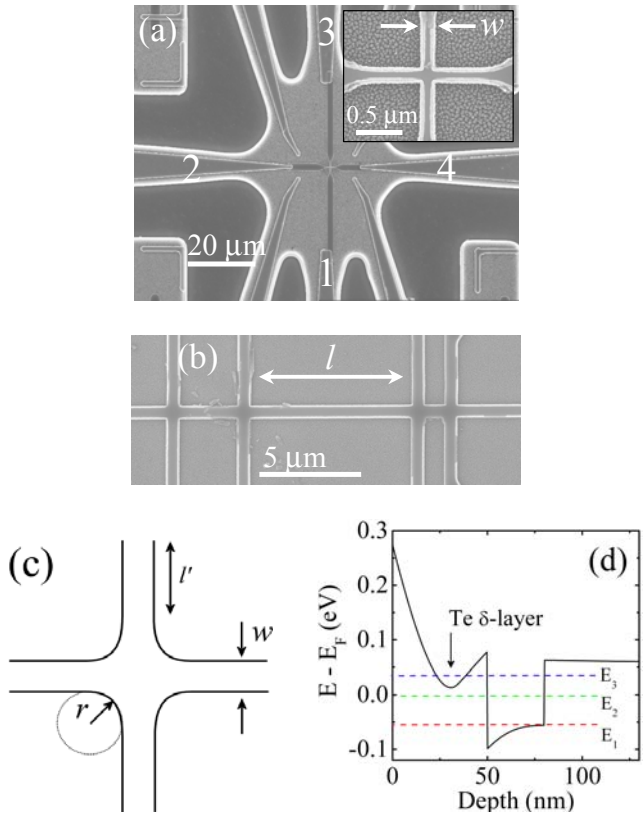

FIG. 1. Electron micrographs of (a) a typical device structure showing the leads and contact arrangement for a cross, and (b) a 550 nm wide Hall bridge. Inset to (a): A w=171 nm cross. (c) A schematic of the Hall cross geometry. (d) A self-consistent Schrödinger-Poisson solution for the conduction band profile of the heterostructure showing the confined energy levels.

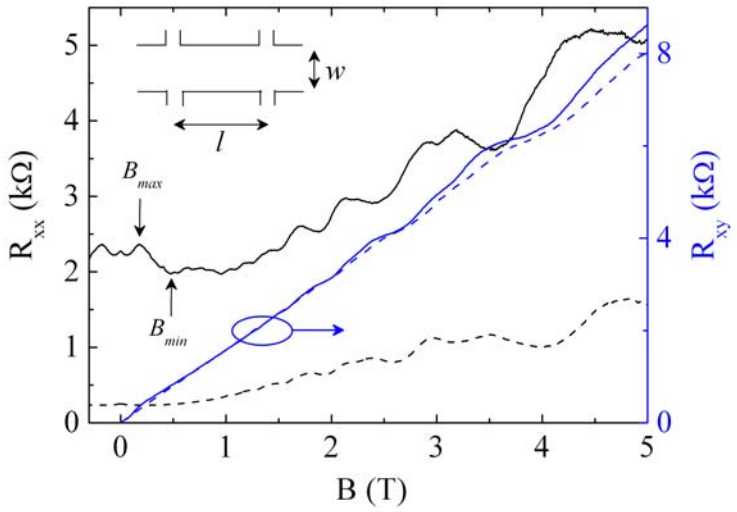

FIG. 2. Longitudinal R_{xx} (left axis) and transverse R_{xy} (right axis) magnetoresistance of w=550 nm (solid lines) and 3 μm (dashed lines) Hall bridges at 2 K (l = 8.4 μm). Inset: A schematic of the device structure and the relevant dimensions. The positions of B_{max} and B_{min} relate to features associated with boundary scattering (see text).

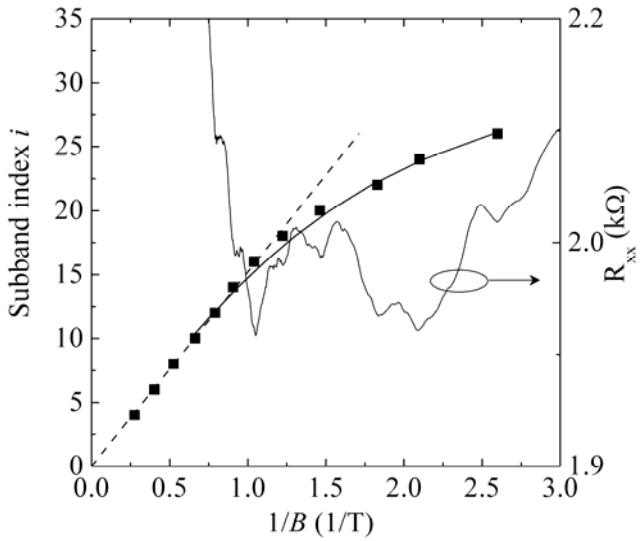

FIG. 3. Subband depopulation diagram for the w=550 nm Hall bridge at 2 K. The faint solid line shows the corresponding R_{xx} data (right hand axis) from which the subband indices (left hand axis) were assigned. The dashed and solid lines represent fits of Eq. 2 to the high field linear portion of the data and the low field non-linear respectively.

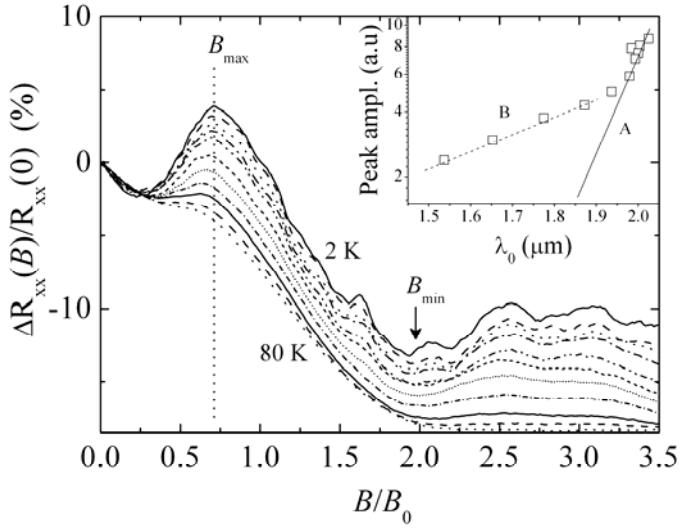

FIG. 4. The magnetoresistance, $\Delta R_{xx}(B)/R_{xx}(0)$, of the w = 550 nm Hall bridge plotted against the normalised field B/B_0, at various temperatures after subtraction of a linear background. Inset: The peak amplitude plotted against the mean free path (λ_0) in the control sample at each temperature.

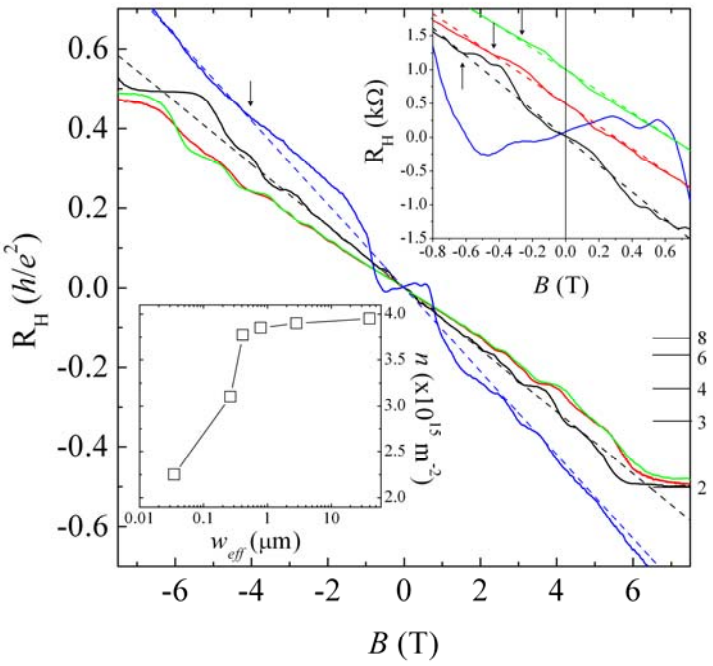

FIG. 5. The Hall resistance R_H in units of h/e^2 as a function of B for a w = 171 nm (blue line), 400 nm (black line), 550 nm (red line), and 924 nm (green line) cross. The dashed lines represent the classical 2D result. Top inset: Low field data illustrating the anomalies in R_H. Data for the w = 550 nm and 924 nm crosses are offset by 0.5 kΩ for clarity. Bottom inset: Dependence of n on the inferred effective width $w_{eff} = w - 2w_{dep}$ of the devices (crosses and bridges).

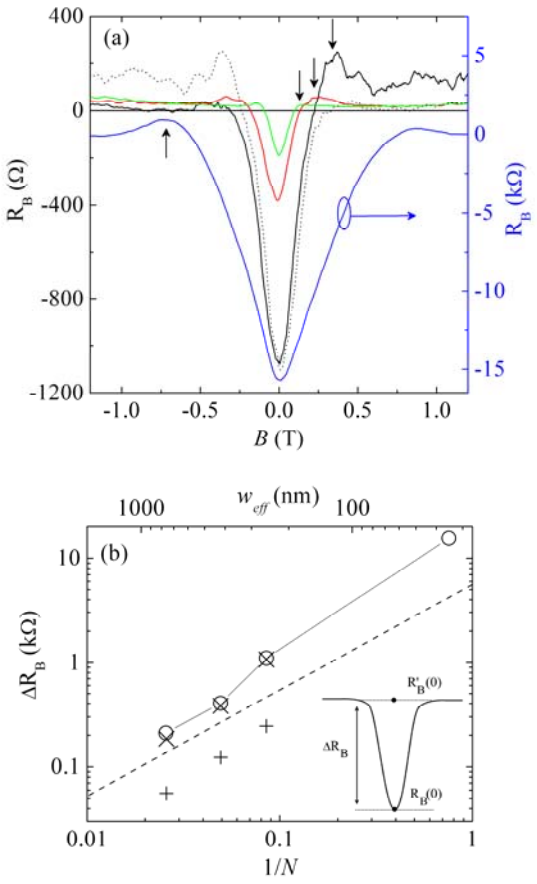

FIG. 6. (a) Bend resistance $R_B = V_{4,3}/I_{1,2}$ as a function of magnetic field for a w = 171 nm (blue line), 400 nm (black line), 550 nm (red line), and 924 nm (green line) cross. The w = 171 nm data is plotted on a difference scale for ease of comparison. The dotted curve is the reciprocal measurement $R_{B'} = V_{1,2}/I_{4,3}$ for the w = 400 nm cross illustrating that asymmetries in B originate from junction asymmetry. (b) Dependence of the experimental NBR amplitude ΔR_B (○) on $1/N = \pi/k_F w_{eff}$ and w_{eff}. The results from billiard model simulations using the parameters given in Table II (x) and results for p = 1 (+) are also shown. The dashed line is a guide to the eye illustrating a $1/N$ dependence. Inset: A schematic showing the definition of ΔR_B.

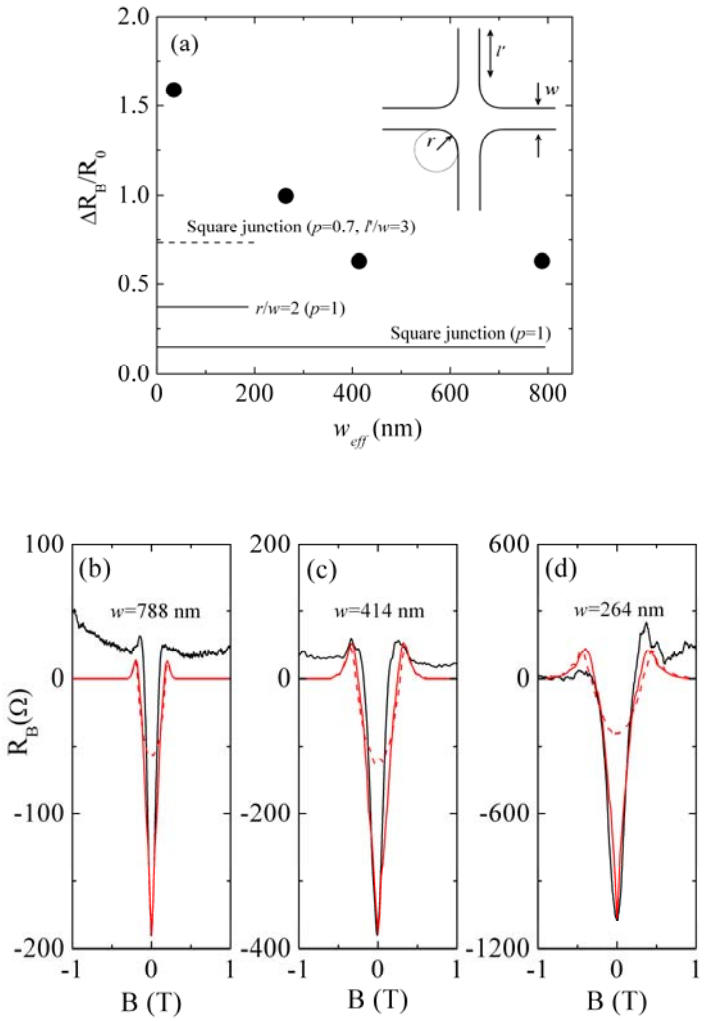

FIG. 7. (a) Normalised NBR amplitude $\Delta R_B/R_0$ of the crosses plotted against w_{eff}. Horizontal lines represent the results from the billiard model for square and rounded junctions with p = 1 (solid lines) along with a square junction with p = 0.7 and l'/w = 3 (dashed line). (b) - (d) Comparisons between experimental R_B (black lines) and billiard model simulations of R_B (solid red lines) for three crosses ($N >> 1$) using parameters listed in Table II. Simulations with p = 1 are shown for comparison (dashed red lines). Inset: A schematic of the geometry used in the simulations. $R_0 = (h/2e^2)(\pi/k_F w_{eff})$.

TABLE I. Properties of the InSb 2DEG obtained from Hall bridges with varying physical width, w at 2 K. Data for w=40 μm represents the control sample. †calculated using the effective electrical width determined in Section IVB.

w (μm)	40	3	0.55
n (10^{15} m^{-2})	3.95	3.9	3.77
μ (m^2/Vs)	19.5	17.95	14.8†
λ_0 (μm)	2.03	1.85	1.50†

TABLE II. Relevant parameters for the ballistic crosses and parameters used in the billiard calculations. Effective widths $w_{eff} = w - 2w_{dep}$ were calculated using $w_{dep} =$ 68 nm determined in Section IVB.

w (nm)	w_{eff} (nm)	n (10^{15} m^{-2})	N	R_0 (Ω)	B_0 (T)	r (nm)	l' (μm)	p
924	788	3.85	39	332	0.13	100	2.5	0.79
550	414	3.77	20.3	638	0.25	100	1.5	0.8
400	264	3.1	11.7	1104	0.35	100	1.2	0.69
171	35	2.25	1.3	9775	2.24	-	0.8	-